ADVANCED ELECTRONIC MATERIALS
www.advelectronicmat.de

Ultrathin Scattering Spin Filter and Magnetic Tunnel Junction Implemented by Ferromagnetic 2D van der Waals Material

Zheng-Zhe Lin and Xi Chen*

Emerging research in 2D materials has promoted the development of nanoelectronics. Ferromagnetic van der Waals (vdW) layered materials can be utilized to implement ultrathin spintronic devices with new functionalities. The theoretical investigation of 2D vdW scattering spin filters and magnetic tunnel junctions consisting of atomically thin Fe_3GeTe_2 (FGT) are reported. By the nonequilibrium Green's function technique, the spin polarization of ballistic transport through single-/double-layer FGT sandwiched between two Cu electrodes is predicted to be 53/85%. In ultrathin FGT-hBN-FGT heterostructures, remarkable magnetoresistance is observed, in which maximum (minimum) resistance occurs when the magnetization of two FGT layers is parallel (antiparallel) to each other. For heterostructures consisting of single-/double-layer FGT, the magnetoresistance reaches 183/252% at zero-bias limit. The parallel state of a FGT magnetic tunnel junction exhibits spin polarization larger than 75%. These results suggest the application of magnetic vdW layered materials in ultrathin spintronics.

1. Introduction

With the rapid development of communication and computing technology, drastic increase in information quantity challenges the writing, saving, and reading of magnetic records. In the past decades, the application of giant magnetoresistance in spintronics has led to a rapid increase in the storage density of magnetic disks. The development of spintronics takes the advantage of electronic spin as a new dimension to be manipulated in devices,[1–3] leading to novel low-power microchip applications. As one of the most promising candidates of spintronic materials, ferromagnetic (FM) semiconductor[4–8] is suggested for spin field-effect transistor which combines logical operation and magnetic storage on a single chip. However, FM semiconductors discovered to date still suffer from too low Curie temperature. The search for room temperature FM semiconductors is still demanding.

In recent years, the development of 2D materials brings new opportunities to spintronics.[9–11] With reduced dimensionality and novel physical properties, 2D layered materials and van der Waals (vdW) heterostructures[12–16] have permeated into many research areas. With d-orbital electrons and easily exfoliated single-layers, FM 2D vdW layered materials become a new research direction of spintronics. For magnetic storage, 2D FM layered materials can greatly enhance the storage density. Nonvolatile electrical control of 2D vdW ferromagnets is proposed as key technology for future magnetoelectric nanodevices.[17] Ideal spintronic materials are required to have Curie temperatures above room temperature, high spin polarization, and high magnetic anisotropy energy (MAE). According to the Mermin–Wagner theorem,[18] 2D long-range FM order cannot exist in an isotropic magnetic system. Recently, people found that 2D layered CrI_3,[19–27] $Cr_2Ge_2Te_6$,[28] and $CrSiTe_3$[29] possesses intrinsic magnetocrystalline anisotropy against thermal fluctuations. However, the Curie temperatures of CrI_3, $Cr_2Ge_2Te_6$, and $CrSiTe_3$ are only dozens of Kelvins. The discovery of Fe_3GeTe_2 (FGT),[30–36] a 2D itinerant ferromagnet with Curie temperature close to room temperature (150–220 K depending on Fe occupancy[33,34,37]), provides a new chance for 2D spintronics. FGT has an advantage on its metallic nature which enables the performance of both electronic spin and charge,[38] and it has been proposed as a rare-earth-free strong magnet with electronic correlation.[39] Recently, a behavior of the tunneling resistance[31] and large anomalous Hall effect[30] were observed in bulk FGT/hBN/FGT heterostructures. A theoretical analysis for the mechanism was then proposed[40] and a very large magnetoresistance was reported. By the doping of ionic gate, the Curie temperature of atomically thin FGT is dramatically elevated to room temperature.[30] The above discovery reveals the possibility of 2D FGT vdW layers serving as an ultrathin spintronic materials.

In this paper, the possibility of atomically thin FGT layers serving as ultrathin scattering spin filter and magnetic tunnel junction is theoretically investigated. Using density functional theory (DFT) calculations and nonequilibrium Green's function technique, the fundamentals of spin-polarized ballistic

Prof. Z.-Z. Lin, Dr. X. Chen
Department of Applied Physics
School of Physics and Optoelectronic Engineering
Xidian University
Xi'an 710071, China
E-mail: zzlin@xidian.edu.cn

The ORCID identification number(s) for the author(s) of this article can be found under https://doi.org/10.1002/aelm.201900968.

DOI: 10.1002/aelm.201900968

transport through single- and double-layer FGT sandwiched between metal electrodes are revealed. High-quality magnetic tunnel junction with remarkable magnetoresistance is realized in ultrathin FGT/hBN/FGT heterostructures. In FGT/hBN/FGT heterostructures sandwiched between metal electrodes consisting of single- and double-layer FGT, typical behavior of tunneling resistance is observed in which maximum/minimum conductance exists when the magnetizations of two FGT layers are parallel/antiparallel to each other. Currents through the parallel states of FGT/hBN/FGT heterostructures present considerable spin polarization. The study preliminarily reveals the possibility of 2D vdW layered ferromagnets as ultrathin spintronic devices, and proposes their applications in future spintronics.

2. Results and Discussion

2.1. Basic Properties of FGT

The structure of single-layer FGT is illustrated in **Figure 1**a. The Fe atoms in one primitive cell are located in two inequivalent Wyckoff sites. Single-layer FGT consists of five sublayers, where the top and bottom contain Te atoms, the second and fourth layers contain Fe_A atoms, the third layer contains Fe_B and Ge atoms. The local density approximation (LDA) functional gives a lattice constant a_0 = 3.89 Å, and a magnetic moment m = 4.55 μ_B of one primitive cell. The magnetic moments of Fe_A/Fe_B are m_A = 1.76 μ_B/m_B = 1.02 μ_B, respectively. LDA predicts the magnetic moment within the range of experimental values (m = 3.60–4.89 μ_B).[32,33] To access the validity of LDA calculations, we also test the Perdew-Burke-Ernzerhof (PBE) functional, and the LDA functional with Hubbard U = 4.54 eV.[39] However, the obtained magnetic moments (m = 6.32/7.16 μ_B for PBE/LDA+U, respectively) are drastically overestimated. This suggests that LDA, which is used throughout this work, is suitable to describe the electronic structure of FGT.

To investigate the electronic properties of single-layer FGT, the spin-up and spin-down band structures without spin-orbit coupling (SOC) are plotted in Figure 1b. The electronic states are projected into Fe 3d, Ge 4p, and Te 5p orbitals. The band feature shows that single-layer FGT is metallic. It can be seen that the states around the Fermi level are dominated by Fe 3d accompany with a few Te 5p orbitals. By projected density of states (PDOS) in Figure 1c, partially occupied Fe 3d bands are observed crossing the Fermi level. This is in accordance with the feature of itinerant ferromagnet. To understand the distribution of magnetic moments, spin density difference (i.e., the difference $\rho_\uparrow - \rho_\downarrow$ of the spin-up and spin-down electron density) is plotted in Figure 1d. The region of spin polarization, with the geometry of $\rho_\uparrow - \rho_\downarrow$ isosurface exhibiting a characteristic of 3d orbitals, further indicates the magnetic moments around Fe atoms.

To reveal the potential ability of FGT in spintronics, MAE is plotted into 3D map in Figure 1e, in which the vector from the center pointing to the 3D map surface depicts the direction of magnetic moment and the value of MAE. The easy axis (z direction) is perpendicular to the surface of FGT. This is consistent with previous experimental observation.[33] With hexagonal symmetry, the MAE of single-layer FGT exhibits uniaxial anisotropy and can be fit to[41]

$$\mathrm{MAE} = K_1 \sin^2\theta + K_2 \sin^4\theta \tag{1}$$

where θ is the angle relative to the easy axis. The resulting magnetocrystalline anisotropy coefficients are K_1 = 2.42 meV per cell and K_2 = 0.04 meV per cell. The maximum MAE, which is defined as the energy difference of the system with magnetization axis along the easy axis and perpendicular to it, is calculated to be 2.46 meV per cell, that is, 0.82 meV per Fe atom. This value is about two orders of magnitude larger than the MAE of Fe, Co, and Ni, and is about one third of the MAE of FePt alloy.[42] The result suggests that single-layer FGT is promising for magnetic storage and spintronic applications.

To further understand the bonding in single-layer FGT, projected Crystal orbital Hamilton population (COHP)[43] of Fe—Fe, Fe—Ge and Fe—Te bonds are calculated. For atomic orbitals $|\mu\rangle$ and $|\nu\rangle$, the projected COHP is defined as

$$\mathrm{COHP}_{\mu\nu}(E) = \sum_{\mathbf{k}j} \langle \mu | \psi_j(\mathbf{k}) \rangle \langle \psi_j(\mathbf{k}) | \nu \rangle \langle \nu | \mathbf{H} | \mu \rangle \delta(E - \varepsilon_j(\mathbf{k})) \tag{2}$$

where $\mathbf{H}$ is the projector augmented wave (PAW) Hamiltonian, $|\psi_j(\mathbf{k})\rangle$ is the j-th Blöch state at the $\mathbf{k}$ point and $\varepsilon_j(\mathbf{k})$ is the energy of $|\psi_j(\mathbf{k})\rangle$. The integrated COHP

$$\mathrm{ICOHP}_{\mu\nu}(E_\mathrm{F}) = \int^{E_\mathrm{F}} \mathrm{COHP}_{\mu\nu}(E)\,\mathrm{d}E \tag{3}$$

to the Fermi level E_F (values listed in **Figure 2**) describes the bonding strength between $|\mu\rangle$ and $|\nu\rangle$. In single-layer FGT, Fe_B atoms are neighboring with Ge atoms, and all the Fe atoms connect to Te atoms. The COHP between Fe_B 3d and Ge 4p orbitals (Figure 2a) has negative values for the energy E deep below E_F, indicating a feature of bonding orbital. For the COHP between Fe 3d and Te 5p orbitals (Figure 2b,c for Fe_A and Fe_B, respectively) bonding feature can be seen for the energy E deep below E_F, accompanying with a little antibonding feature near E_F. This is consistent with the projected band structure in Figure 1b. where a few Te 5p components are resolved near E_F. The large negative ICOHP(E_F) values of Fe 3d-Ge 4p and Fe 3d-Te 5p bonds indicate that these strong bonds support the structure of single-layer FGT. By contrast, the Fe—Fe bonding is weaker ((Figure 2d,f), with less negative ICOHP(E_F)). The coupling between Fe_A 3d orbitals presents antibonding feature around the Fermi level E_F (Figure 2d). To understand these orbitals, local density of states

$$\mathrm{LDOS}(\mathbf{r}, E) = \sum_{\mathbf{k}j} |\psi_j(\mathbf{k})|^2 \delta(E - \varepsilon_j(\mathbf{k})) \tag{4}$$

at the Fermi level E_F is depicted in Figure 2e. The electron distribution exhibits a characteristic of antibonding orbitals between Fe_A atoms (corresponding to the large positive COHP near E_F in Figure 2d). This may be attributed to spin polarization in FGT, in which Fe 3d electrons with majority spin fill more orbitals than minority spin and then occupy higher states

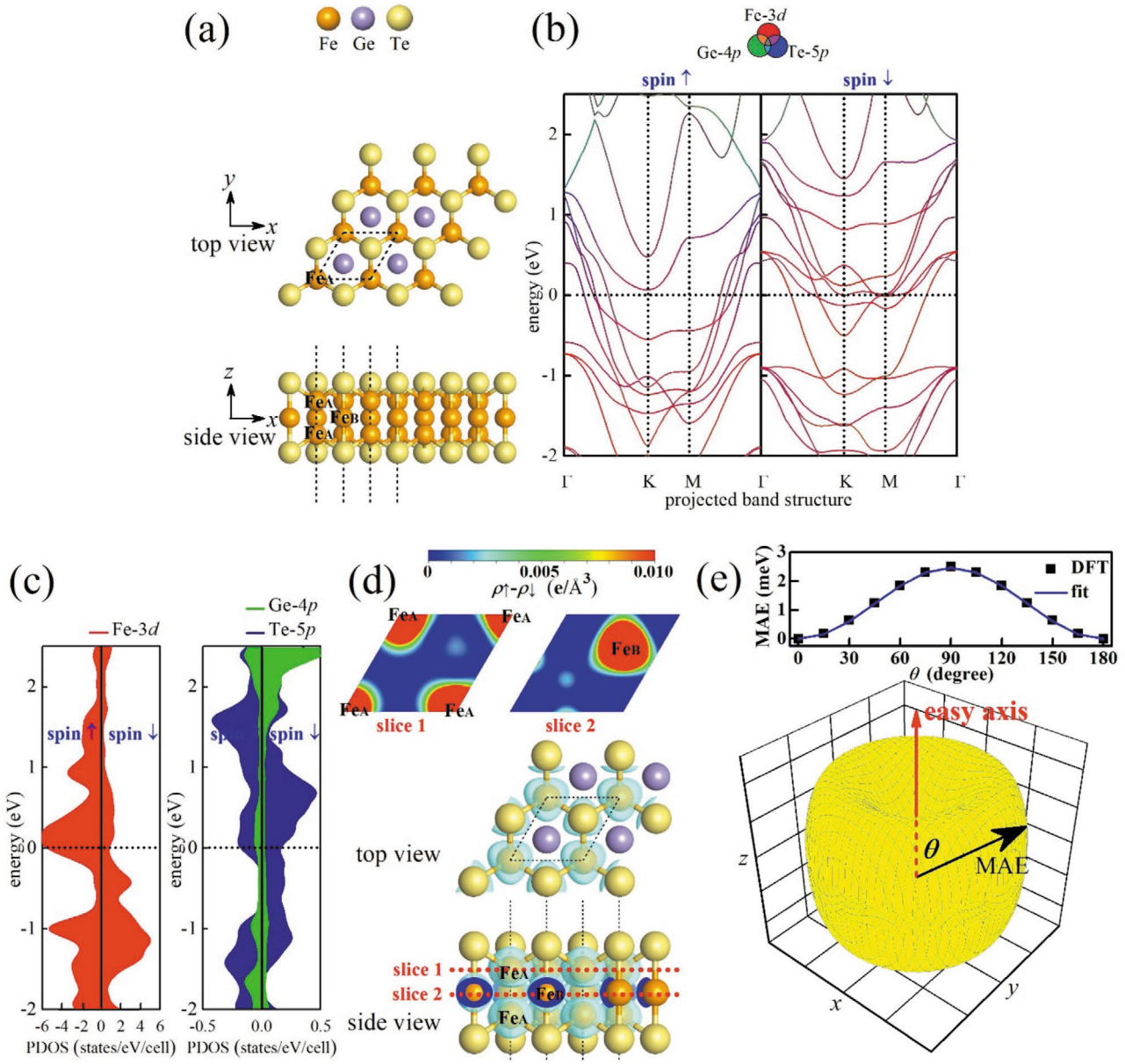

Figure 1. Electronic properties of single-layer FGT. a) The atomic structure of single-layer FGT. The unit cell is enclosed by the dashed lines. Inequivalent Fe atoms are denoted by Fe_A and Fe_B. b) Orbital-resolved spin-up and spin-down band structures of single-layer FGT. The red, green, and blue projections come from Fe 3d, Ge 4p, and Te 5p orbitals, respectively. c) PDOS of single-layer FGT. d) The isosurfaces plot the spin density difference in single-layer FGT with value of $\rho_\uparrow - \rho_\downarrow = 3 \times 10^{-3}$ e Å^{-3}. The color maps plot $\rho_\uparrow - \rho_\downarrow$ in two horizontal slices. e) 3D map for MAE of single-layer FGT. The direction of the vector illustrates the spin direction. The length of the vector illustrates the value of MAE. The upper panel plots MAE varying with angle θ.

in energy bands. The spin-polarized electrons near E_F center on Fe_A 3d orbitals on the surface of single-layer FGT, and make a major contribution to the spin-polarized conduction.

2.2. Scattering Spin Filter by Atomically Thin FGT

In this section, we investigate the possibility of atomically thin FGT serving as ultrathin scattering spin filter. We first consider single-layer FGT sandwiched between two Cu electrodes which have small lattice mismatch with FGT crystal. Since FGT is a metal, the Cu-FGT-Cu structure is different from classical metal–semiconductor/insulator–metal spin filter. Electrons passing through the Cu-FGT-Cu structure feel potential wells whose depths are spin dependent. In the two-probe system, $\sqrt{3} \times \sqrt{3}$ Cu (111) surface (a = 4.43 Å) is matched with 1 × 1 single-layer FGT (a_0 = 3.89 Å) (Figure S1, Supporting Information). Geometry relaxation to the Cu-FGT-Cu system (**Figure 3**a) results in a compromised lateral lattice constant a = 4.22 Å, in which the lattice mismatch for Cu/FGT is −5%/+8%,

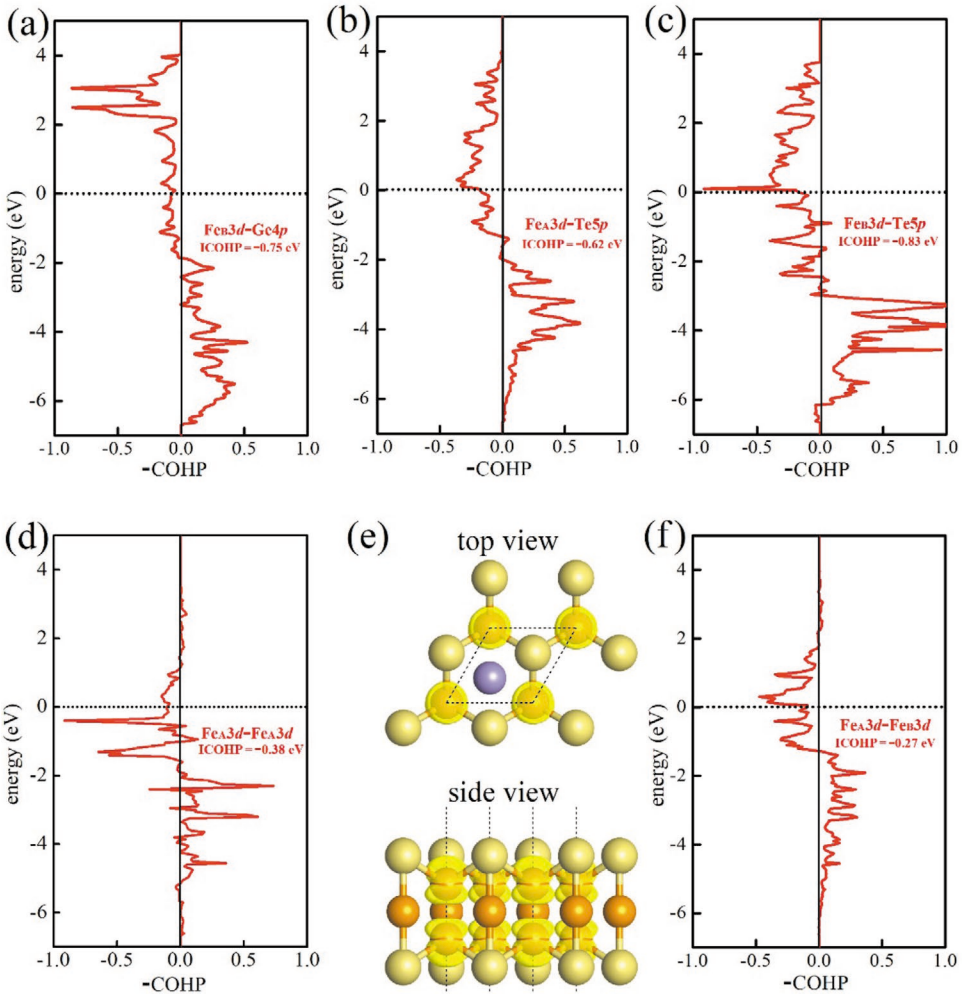

Figure 2. COHP of the bonds in single-layer FGT. a) COHP of bonding between Fe_B 3d and Ge 4p orbitals. b) COHP of bonding between Fe_A 3d and Te 5p orbitals. c) COHP of bonding between Fe_B 3d and Te 5p orbitals. d) COHP of bonding between Fe_A 3d orbitals. e) Isosurfaces of LDOS(**r**, E_F) at the Fermi level with value of 0.02 $Å^{-3}$ eV^{-1}. f) COHP of bonding between Fe_A 3d and Fe_B 3d orbitals.

respectively. The distance from FGT surface Te atoms to Cu surface layer is about 2.3 Å, which is larger than the distances between the atomic layers in Cu bulk. On the basis of DFT total energies, the adsorption energy of FGT on Cu surface, which is defined as

$$E_{ads} = \frac{1}{2}\left(E_{DFT}(FGT) + 2E_{DFT}(Cu) - E_{DFT}(Cu-FGT-Cu)\right) \quad (5)$$

is estimated to be 1.27 eV per FGT cell.

The spin density difference $\rho_\uparrow - \rho_\downarrow$ of the system is shown in Figure 3b. It can be seen that the magnetic moments localized around Fe atoms consist of spin-polarized electronic channels. Using nonequilibrium Green's function method, we obtain the transmission spectrum of Cu-FGT-Cu system under zero bias (Figure 3c). The ballistic transport near the Fermi level shows obvious spin polarization. Under the given bias voltage, the spin-up (spin-down) current $I_\uparrow$ ($I_\downarrow$) can be evaluated by the Landauer–Büttiker formula (Figure 3d). The spin polarization of current is defined as

$$P = \left|I_\uparrow - I_\downarrow\right| / \left(I_\uparrow + I_\downarrow\right) \quad (6)$$

Figure 3e plots the spin polarization of current with bias voltage. At zero bias, the polarization reaches 53%. In the range of 0–0.3 V, the polarization keeps close to that of 0 V. With increasing bias voltage, the polarization declines to 30% at 1.0 V. The results indicate that single-layer FGT is a suitable material for ultrathin scattering spin filter.

To understand the mechanism of spin filtering, we explore into the exchange and correlation between electrons in thin FGT layer. In the framework of DFT, a physical picture of near-free electrons is employed to describe the interactions. In the single-electron Schrödinger equations of DFT, the dynamic interaction between electrons are included in effective exchange-correlation potential $V_{XC\ \sigma}$, which is relative to electron spin σ. Electrons passing through FGT feel effective barriers which are dependent on spin. By the intrinsic magnetism of FGT, spin-up and spin-down electrons climb over different barrier heights. To reveal such difference, Figure 3f plots $V_{XC\uparrow} - V_{XC\downarrow}$ on a slice plane cutting through the three Fe

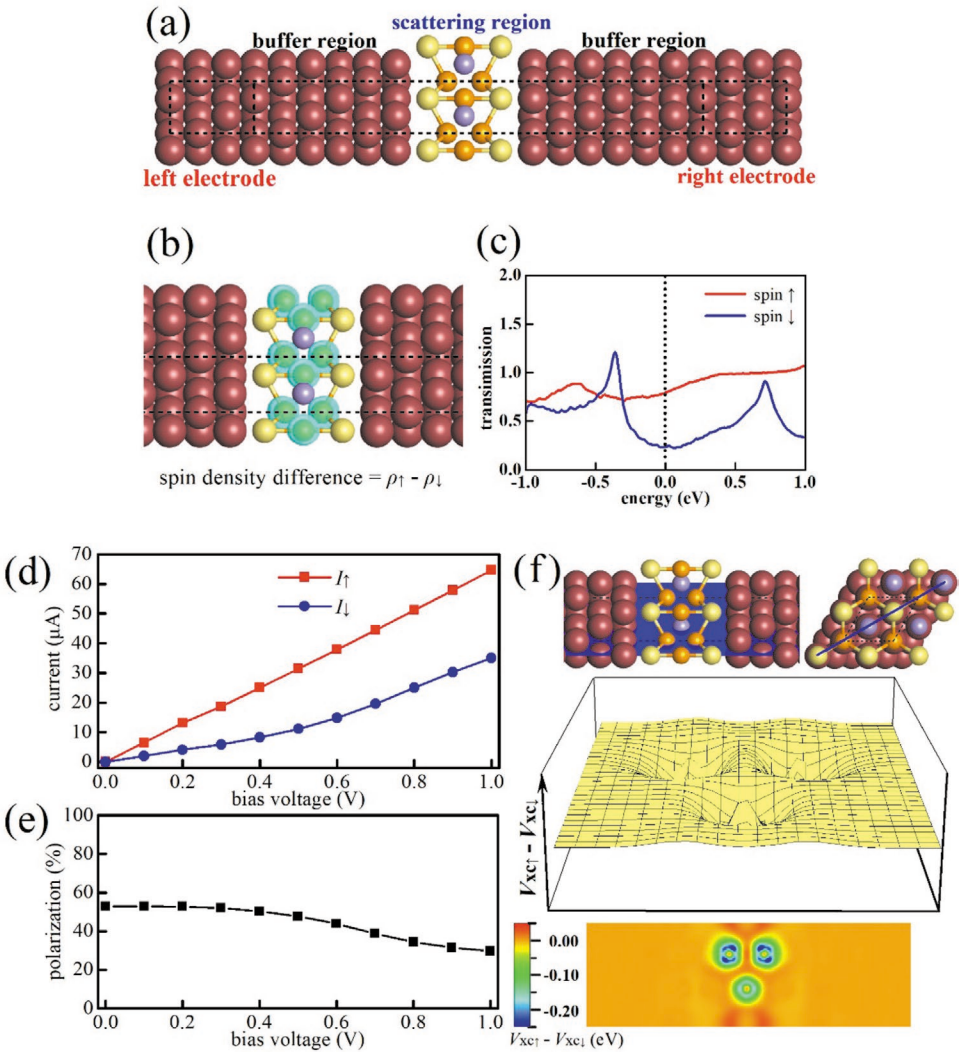

Figure 3. Single-layer FGT scattering spin filter sandwiched between two Cu electrodes. a) Two-probe model for nonequilibrium Green's function calculations. b) Isosurfaces of spin density with value of $\rho_\uparrow - \rho_\downarrow = 5 \times 10^{-3}$ e Å^{-3}. c) Transmission spectrum of Cu-FGT-Cu system under zero bias. The Fermi energy is set zero. d) Spin-up current $I_\uparrow$ and spin-down current $I_\downarrow$ varying with bias voltage. e) Spin polarization of current varying with bias voltage. f) The difference $V_{XC\uparrow} - V_{XC\downarrow}$ between spin-up and spin-down exchange-correlation potentials in Cu-FGT-Cu system. The 2D and 3D maps are plotted on the slice plane shown by blue color.

atoms in the Cu-FGT-Cu system. Obvious difference between $V_{XC\uparrow}$ and $V_{XC\downarrow}$ is observed in the region near Fe atoms. Such difference on V_{XC} results in a difference of scattering probability between spin-up and spin-down electrons.

To enhance the effect of spin filtering, we further investigate double-layer FGT sandwiched between Cu electrodes (**Figure 4**a). The stacking of two FGT layers is taken as that in bulk FGT. This system also shows spin density difference $\rho_\uparrow - \rho_\downarrow$ around Fe atoms (Figure 4b). The ballistic transport near the Fermi level also shows obvious spin polarization (Figure 4c). According to the calculation results of spin-up and spin-down currents (Figure 4d), the polarization (Figure 4e) is found to be higher than the system with single-layer FGT. At zero bias, the polarization reaches 85%. With increasing bias voltage, the polarization declines to 53% at 1.0 V. The results indicate that double-layer FGT is more suitable than single-layer FGT for ultra-thin scattering spin filter.

2.3. Magnetic Tunnel Junction by Atomically Thin FGT

In this section, we exhibit the ability of atomically thin FGT as material of ultrathin magnetic tunnel junction. We start from single-layer FGT. **Figure 5**a displays the model of single-layer FGT-hBN-FGT heterostructure sandwiched between two Cu electrodes. The single-layer hBN acts as a thin insulting layer separating conducting parts on both sides. The on/off state of the system is controlled by manipulating the directions of magnetic moments in two FGT layers. The parallel state, in which the directions of both magnetic moments are in the same direction (the insets in Figure 5b), corresponds to the turn on state. The antiparallel state, in which the directions of magnetic moments are opposite (the insets in Figure 5c), corresponds to the turn off state. At the parallel state, the ballistic transport near the Fermi level also shows obvious spin polarization (Figure 5b). At the antiparallel state, the transmission near the Fermi level is much

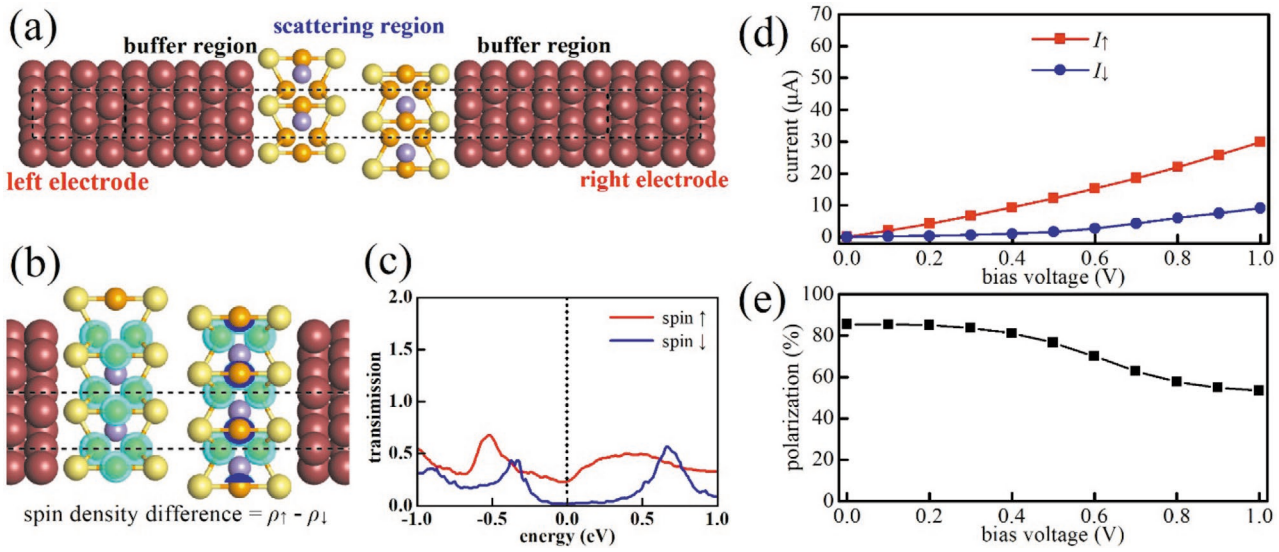

Figure 4. Double-layer FGT scattering spin filter sandwiched between two Cu electrodes. a) Two-probe model for nonequilibrium Green's function calculations. b) Isosurfaces of spin density with value of $\rho_{\uparrow} - \rho_{\downarrow} = 5 \times 10^{-3}$ e Å^{-3}. c) Transmission spectrum of Cu-FGT-Cu system under zero bias. The Fermi energy is set zero. d) Spin-up current $I_{\uparrow}$ and spin-down current $I_{\downarrow}$ varying with bias voltage. e) Spin polarization of current varying with bias voltage.

lower (Figure 5c). For parallel and antiparallel states, we calculate the total currents $I_P = I_{P\uparrow} + I_{P\downarrow}$ and $I_{AP} = I_{AP\uparrow} + I_{AP\downarrow}$. Figure 5d shows that $I_P > I_{AP}$ under bias voltage 0.0–1.0 V.

Having established the behavior of single-layer FGT-hBN-FGT heterostructure as magnetic tunnel junction, we now focus on its tunneling magnetoresistance (TMR) which is defined as

$$\mathrm{TMR} = \frac{R_{AP} - R_P}{R_P} = \frac{1/I_{AP} - 1/I_P}{1/I_P} \tag{7}$$

where R_P and R_{AP} represent the resistance of parallel and antiparallel states. Figure 5e exhibits TMR varying with bias voltage. At zero bias, TMR reaches a maximum of 183%. With increasing voltage, TMR gradually decreases to 78% at 1.0 V. We also examine the TMR of two bulks of FGT separated by hBN (Figure S2, Supporting Information), obtaining a TMR of 289% at zero bias voltage (Figure S2e, Supporting Information). It is worth noting that our value is closer to the experimental value[31] than ref. [40] Here, the two-probe model for mesoscopic electronic scattering is closer to the experimental setup, and thus we infer that our simulation could give reliable results in accordance with the actual situation. By contrast, the TMR of single-layer FGT-hBN-FGT heterostructure is comparable with that of bulk FGT. At the parallel state, single-layer FGT-hBN-FGT heterostructure presents a behavior of spin filtering with a polarization of 79% at zero bias (Figure S3, Supporting Information).

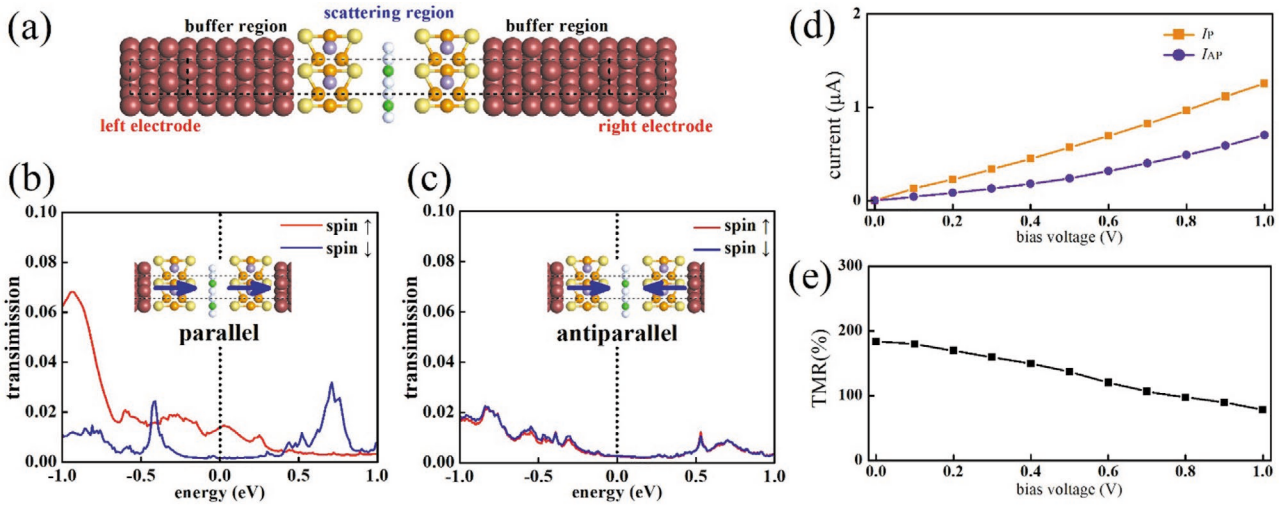

Figure 5. Single-layer FGT-hBN-FGT magnetic tunnel junction sandwiched between two Cu electrodes. a) Two-probe model for nonequilibrium Green's function calculations. b) Transmission spectrum of the system at the parallel state under zero bias. c) Transmission spectrum of the system at the antiparallel state under zero bias. d) Total current I_P at the parallel state and I_{AP} at the antiparallel state varying with bias voltage. e) TMR varying with bias voltage.

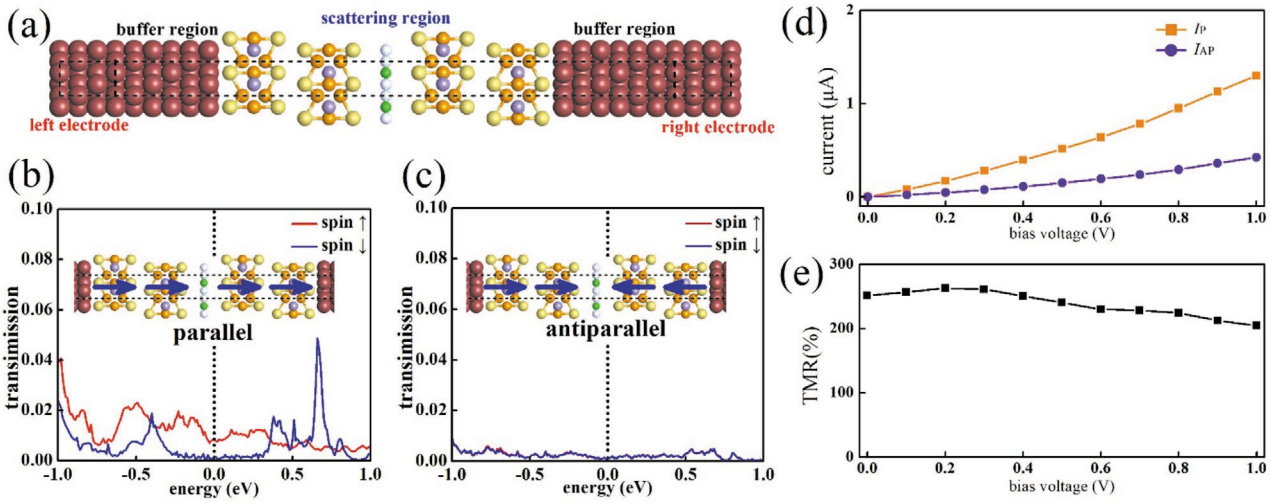

Figure 6. Double-layer FGT-hBN-FGT magnetic tunnel junction sandwiched between two Cu electrodes. a) Two-probe model for nonequilibrium Green's function calculations. b) Transmission spectrum of the system at the parallel state under zero bias. c) Transmission spectrum of the system at the antiparallel state under zero bias. d) Total current I_P at the parallel state and I_{AP} at antiparallel state varying with bias voltage. e) TMR varying with bias voltage.

The TMR of such FGT-hBN-FGT heterostructure originates from the ferromagnetism of two thin FGT layers, which is different from the bulk FGT in experiments[31] and results in different spin polarization and TMR.

To achieve larger TMR, we then focus on double-layer FGT-hBN-FGT heterostructure sandwiched between two Cu electrodes (**Figure 6**a). The transmission spectra of parallel and antiparallel states are shown in Figures 6b and6c, respectively. The antiparallel state exhibits very low transmission near the Fermi level, implying that the TMR would be larger. The total currents of parallel and antiparallel states varying with bias voltage are plotted in Figure 6d. At zero bias voltage, the TMR reaches 252% (Figure 6e), which is larger than that of single-layer FGT-hBN-FGT heterostructure. At the parallel state, double-layer FGT-hBN-FGT heterostructure presents a behavior of spin filtering with a polarization of 76% at zero bias (Figure S4, Supporting Information). Overall, double-layer FGT is suitable for ultrathin magnetic tunnel junctions, with a TMR that is even close to that of bulk FGT.

It is worth noting that the TMR of FGT-hBN-FGT heterostructures is inconsistent with Julliere's model. Julliere's model supposes that the TMR originates from the spin polarization of electrodes. The spin currents are from spin-up to spin-up and spin-down to spin-down transfer between electrodes. Thus, we have $I_P = D_\uparrow D_\uparrow + D_\downarrow D_\downarrow$ and $I_{AP} = D_\uparrow D_\downarrow + D_\downarrow D_\uparrow$, where $D_\uparrow$ and $D_\downarrow$ are the spin-up and spin-down density of states in the Fermi level of electrode. Then one gets

$$\mathrm{TMR}_{\mathrm{julliere}} = \frac{1/I_{AP} - 1/I_P}{1/I_P} = \frac{2P^2}{1-P^2} \tag{8}$$

where $P = (D_\uparrow - D_\downarrow)/(D_\uparrow + D_\downarrow)$ is the spin polarization of electrode. For single- /double-layer FGT-hBN-FGT heterostructures, P = 53/85% lead to $\mathrm{TMR}_{\mathrm{julliere}}$ = 78/520% which are different from previous calculated values 183/252%, respectively. Here, we notice that the spin currents of FGT-hBN-FGT heterostructures originates from the spin-dependent scattering of FGT layers. This mechanism is different from ordinary magnetic tunnel junctions, and a new model is then proposed. For a 1D potential $U = U(z)$, the WKB approximation provides a transmission $T = \exp\left(-\frac{2}{\hbar}\int \sqrt{2m(U(z)-E_F)}\,dz\right)$. According to this exponential rule, for electrons passing through two neighboring scattering layers, the total transmission $T = T_1T_2$ is the product of two separate transmission T_1 and T_2. In Figure 3f, we have pointed out that spin-dependent scattering potential for electrons. Then the total transmission for parallel and antiparallel states are $T_{P\uparrow} = T_\uparrow{}^2$, $T_{P\downarrow} = T_\downarrow{}^2$, and $T_{AP\uparrow} = T_{AP\downarrow} = T_\uparrow T_\downarrow = \sqrt{T_{P\uparrow}T_{P\downarrow}}$. The total currents should be $I_P = K(T_\uparrow T_\uparrow + T_\downarrow T_\downarrow)$ and $I_{AP} = K(T_\uparrow T_\downarrow + T_\downarrow T_\uparrow)$. Finally, we get

$$\mathrm{TMR}_{\mathrm{scattering}} = \frac{1/I_{AP} - 1/I_P}{1/I_P} = \frac{(T_\uparrow - T_\downarrow)^2}{2T_\uparrow T_\downarrow}. \tag{9}$$

For single-layer FGT-hBN-FGT heterostructure, the calculated transmission $T_{P\uparrow} = 1.3 \times 10^{-2}$, $T_{P\downarrow} = 1.0 \times 10^{-3}$, and $T_{AP\uparrow} = T_{AP\downarrow} = 2.5 \times 10^{-3}$ indeed fit $T_{AP\uparrow} \approx \sqrt{T_{P\uparrow}T_{P\downarrow}}$. Then we can infer that $T_\uparrow = \sqrt{T_{P\uparrow}} = 1.1 \times 10^{-1}$ and $T_\downarrow = \sqrt{T_{P\downarrow}} = 2.2 \times 10^{-2}$, and the calculated $\mathrm{TMR}_{\mathrm{scattering}}$ = 160% is close to the value in previous simulation. For double-layer FGT-hBN-FGT heterostructure, the calculated transmission $T_{P\uparrow} = 8.4 \times 10^{-3}$, $T_{P\downarrow} = 1.0 \times 10^{-3}$, and $T_{AP\uparrow} = T_{AP\downarrow} = 1.4 \times 10^{-3}$ also fit $T_{AP\uparrow} \approx \sqrt{T_{P\uparrow}T_{P\downarrow}}$. Then we can infer that $T_\uparrow = \sqrt{T_{P\uparrow}} = 9.2 \times 10^{-2}$ and $T_\downarrow = \sqrt{T_{P\downarrow}} = 1.5 \times 10^{-2}$, and the calculated $\mathrm{TMR}_{\mathrm{scattering}}$ = 215% is close to the value in previous simulation. Overall, our assumption exists and the rule for I_P and I_{AP} can be explained.

3. Conclusion

In this work, the possibility of atomically thin FGT layers serving as materials for ultrathin scattering spin filters and magnetic tunnel junctions is theoretically explored. Analysis based on DFT reveals the intrinsic magnetism of itinerant

3d electrons in layered FGT. The itinerant electrons up to the Fermi level raise the ferromagnetism of FGT and constitute spin-polarized channels for spin filtering and spin value. The ballistic transport through atomically thin FGT exhibits large spin polarization. Remarkable TMR can be achieved in ultrathin FGT-hBN-FGT heterostructures, in which maximum/minimum conductance occurs when the magnetizations of two FGT layers are parallel/antiparallel to each other. The TMR of double-layer FGT-hBN-FGT heterostructures is even close to that of two FGT bulks separated by hBN. Our results reveal the possibility of 2D layered ferromagnets applied in ultrathin spintronic devices and future spintronics.

4. Experimental Section

The DFT calculations were performed with the PAW method,[44,45] as implemented in the Vienna ab initio simulation package (VASP)[46–49] within the LDA.[50] The correction of vdW interactions was treated by the DFT-D3 method with Becke–Jonson damping.[51,52] To verify the reliability, comparison calculations using the PBE[53] and the LDA functional with effective Hubbard U parameter were also performed.[54] Plane-wave basis set was used with a kinetic energy cutoff of 500 eV. The Brillouin zone integration was performed with a $15 \times 15 \times 1$ Γ-centered Monkhorst–Pack grid. The convergence of total energy was considered to be achieved until the total energy difference of two iterated steps was less than 10^{-5} eV. To sufficiently reduce the interlayer interactions, the replicas of simulation system were separated by a vacuum spacing of at least 15 Å in the direction perpendicular to the 2D surface. The atomic positions were fully relaxed until the Hellmann–Feynman forces were below 0.01 eV $Å^{-1}$. To calculate the MAE, the SOC was included in the computation with a full k-point grid.

COHP analysis was carried out with the LOBSTER package.[43,55–57] The pbeVaspFit2015 basis was used with the following basis functions: Fe: 3d, 4s, and 4p; Ge: 4s and 4p; Te: 5s and 5p. The wavefunctions were obtained from the DFT calculations within LDA.

Quantum transport calculations were performed using nonequilibrium Green's function method[58] implemented in the TRANSIESTA code.[59] The LDA functional[50] and the improved Troullier–Martins pseudopotentials[60] were employed. Valence electrons were described by double-ζ plus polarization basis set with the grid mesh cutoff set 250 Ry. The Brillouin zone of electrodes was sampled by $15 \times 15 \times 100$ Monkhorst–Pack grid. For a bias voltage V_b applied on the z direction, the current I_σ was given by the Landauer–Büttiker formula[61]

$$I_\sigma = \frac{2e}{h}\int T_\sigma(E,V_b)\left[f_L\left(E - E_F - \frac{eV_b}{2}\right) - f_R\left(E - E_F + \frac{eV_b}{2}\right)\right]dE \quad (10)$$

where $\sigma = \pm 1$ denotes spin-up/spin-down, $T_\sigma(E, V_b)$ is the transmission, E_F is the Fermi energy, and f_L/f_R are the Fermi–Dirac distribution of left/right electrodes at room temperature.

Supporting Information

Supporting Information is available from the Wiley Online Library or from the author.

Acknowledgements

This work was supported by the National Natural Science Foundation of China (No. 11847047), the Natural Science Basic Research plan in Shaanxi Province of China (No. 2018JQ1034), the Fundamental Research Funds for the Central Universities (Nos. JB180513 and XJS18038), and Postdoctoral Research Project of Shaanxi Province.

Conflict of Interest

The authors declare no conflict of interest.

Keywords

2D ferromagnetism, magnetic tunnel junctions, spin filters

Received: September 6, 2019
Revised: December 22, 2019
Published online: January 29, 2020

[1] A. Fert, *Rev. Mod. Phys.* **2008**, *80*, 1517.
[2] S. A. Wolf, D. D. Awschalom, R. A. Buhrman, J. M. Daughton, S. von Molnar, M. L. Roukes, A. Y. Chtchelkanova, D. M. Treger, *Science* **2001**, *294*, 1488.
[3] S. Bhatti, R. Sbiaa, A. Hirohata, H. Ohno, S. Fukami, S. N. Piramanayagam, *Mater. Today* **2017**, *20*, 530.
[4] S. von Molnar, S. Methfessel, *J. Appl. Phys.* **1968**, *39*, 899.
[5] H. Munekata, H. Ohno, S. von Molnar, A. Segmüller, L. L. Chang, L. Esaki, *Phys. Rev. Lett.* **1989**, *63*, 1849.
[6] T. Dietl, *Nat. Mater.* **2010**, *9*, 965.
[7] Y. Matsumoto, M. Murakami, T. Shono, T. Hasegawa, T. Fukumura, M. Kawasaki, P. Ahmet, T. Chikyow, S.-y. Koshihara, H. Koinuma, *Science* **2001**, *291*, 854.
[8] A. Shen, H. Ohno, F. Matsukura, Y. Sugawara, N. Akiba, T. Kuroiwa, A. Oiwa, A. Endo, S. Katsumoto, Y. Iye, *J. Cryst. Growth* **1997**, *175-176*, 1069.
[9] M. Gibertini, M. Koperski, A. F. Morpurgo, K. S. Novoselov, *Nat. Nanotechnol.* **2019**, *14*, 408.
[10] L. Thiel, Z. Wang, M. A. Tschudin, D. Rohner, I. Gutierrez-Lezama, N. Ubrig, M. Gibertini, E. Giannini, A. F. Morpurgo, P. Maletinsky, *Science* **2019**, *364*, 973.
[11] C. Cardoso, D. Soriano, N. A. Garcia-Martinez, J. Fernandez-Rossier, *Phys. Rev. Lett.* **2018**, *121*, 067701.
[12] K. Kang, K.-H. Lee, Y. Han, H. Gao, S. Xie, D. A. Muller, J. Park, *Nature* **2017**, *550*, 229.
[13] M.-Y. Li, Y. Shi, C.-C. Cheng, L.-S. Lu, Y.-C. Lin, H.-L. Tang, M.-L. Tsai, C.-W. Chu, K.-H. Wei, J.-H. He, W.-H. Chang, K. Suenaga, L.-J. Li, *Science* **2015**, *349*, 524.
[14] R. Ribeiro-Palau, C. Zhang, K. Watanabe, T. Taniguchi, J. Hone, C. R. Dean, *Science* **2018**, *361*, 690.
[15] W. Xu, W. Liu, J. F. Schmidt, W. Zhao, X. Lu, T. Raab, C. Diederichs, W. Gao, D. V. Seletskiy, Q. Xiong, *Nature* **2017**, *541*, 62.
[16] Z. Yu, Z.-Y. Ong, S. Li, J.-B. Xu, G. Zhang, Y.-W. Zhang, Y. Shi, X. Wang, *Adv. Funct. Mater.* **2017**, *27*, 1604093.
[17] Y. Zhao, J.-J. Zhang, S. Yuan, Z. Chen, *Adv. Funct. Mater.* **2019**, *29*, 1901420.
[18] N. D. Mermin, H. Wagner, *Phys. Rev. Lett.* **1966**, *17*, 1133.
[19] P. Jiang, C. Wang, D. Chen, Z. Zhong, Z. Yuan, Z.-Y. Lu, W. Ji, *Phys. Rev. B* **2019**, *99*, 144401.
[20] H. H. Kim, B. Yang, T. Patel, F. Sfigakis, C. Li, S. Tian, H. Lei, A. W. Tsen, *Nano Lett.* **2018**, *18*, 4885.
[21] T. Song, X. Cai, M. W.-Y. Tu, X. Zhang, B. Huang, N. P. Wilson, K. L. Seyler, L. Zhu, T. Taniguchi, K. Watanabe, M. A. McGuire, D. H. Cobden, D. Xiao, W. Yao, X. Xu, *Science* **2018**, *360*, 1214.

[22] Z. Wang, I. Gutierrez-Lezama, N. Ubrig, M. Kroner, M. Gibertini, T. Taniguchi, K. Watanabe, A. Imamoğlu, E. Giannini, A. F. Morpurgo, *Nat. Commun.* **2018**, *9*, 2516.
[23] N. Sivadas, S. Okamoto, X. Xu, C. J. Fennie, D. Xiao, *Nano Lett.* **2018**, *18*, 7658.
[24] P. H. Jian, L. Li, Z. L. Liao, Y. X. Zhao, Z. C. Zhong, *Nano Lett.* **2018**, *18*, 3844.
[25] W. Jin, H. H. Kim, Z. Ye, S. Li, P. Rezaie, F. Diaz, S. Siddiq, E. Wauer, B. Yang, C. Li, S. Tian, K. Sun, H. Lei, A. W. Tsen, L. Zhao, R. He, *Nat. Commun.* **2018**, *9*, 5122.
[26] H. H. Kim, B. Yang, S. Tian, C. Li, G.-X. Miao, H. Lei, A. W. Tsen, *Nano Lett.* **2019**, *19*, 5739.
[27] T. Song, M. W.-Y. Tu, C. Carnahan, X. Cai, T. Taniguchi, K. Watanabe, M. A. McGuire, D. H. Cobden, D. Xiao, W. Yao, X. Xu, *Nano Lett.* **2019**, *19*, 915.
[28] C. Gong, L. Li, Z. Li, H. Ji, A. Stern, Y. Xia, T. Cao, W. Bao, C. Wang, Y. Wang, Z. Q. Qiu, R. J. Cava, S. G. Louie, J. Xia, X. Zhang, *Nature* **2017**, *546*, 265.
[29] J. Zhang, X. Cai, W. Xia, A. Liang, J. Huang, C. Wang, L. Yang, H. Yuan, Y. Chen, S. Zhang, Y. Guo, Z. Liu, G. Li, *Phys. Rev. Lett.* **2019**, *123*, 047203.
[30] Y. Deng, Y. Yu, Y. Song, J. Zhang, N. Z. Wang, Z. Sun, Y. Yi, Y. Z. Wu, S. Wu, J. Zhu, J. Wang, X. H. Chen, Y. Zhang, *Nature* **2018**, *563*, 94.
[31] Z. Wang, D. Sapkota, T. Taniguchi, K. Watanabe, D. Mandrus, A. F. Morpurgo, *Nano Lett.* **2018**, *18*, 4303.
[32] B. Chen, J. Yang, H. Wang, M. Imai, H. Ohta, C. Michioka, K. Yoshimura, M. Fang, *J. Phys. Soc. Jpn.* **2013**, *82*, 124711.
[33] H. J. Deiseroth, K. Aleksandrov, C. Reiner, L. Kienle, R. K. Kremer, *Eur. J. Inorg. Chem.* **2006**, *2006*, 1561.
[34] A. F. May, S. Calder, C. Cantoni, H. Cao, M. A. McGuire, *Phys. Rev. B* **2016**, *93*, 014411.
[35] C. K. Tian, C. Wang, W. Ji, J. C. Wang, T. L. Xia, L. Wang, J.-J. Liu, H.-X. Zhang, P. Cheng, *Phys. Rev. B* **2019**, *99*, 184428.
[36] Z. Y. Fei, B. Huang, P. Malinowski, W. B. Wang, T. C. Song, J. Sanchez, W. Yao, D. Xiao, X. Zhu, A. F. May, W. Wu, D. H. Cobden, J.-H. Chu, X. Xu, *Nat. Mater.* **2018**, *17*, 778.
[37] S. Liu, X. Yuan, Y. Zou, Y. Sheng, C. Huang, E. Zhang, J. Ling, Y. Liu, W. Wang, C. Zhang, J. Zou, K. Wang, F. Xiu, *npj 2D Mater. Appl.* **2017**, *1*, 30.
[38] H. L. Zhuang, P. R. C. Kent, R. G. Hennig, *Phys. Rev. B* **2016**, *93*, 134407.
[39] J.-X. Zhu, M. Janoschek, D. S. Chaves, J. C. Cezar, T. Durakiewicz, F. Ronning, Y. Sassa, M. Mansson, B. L. Scott, N. Wakeham, E. D. Bauer, J. D. Thompson, *Phys. Rev. B* **2016**, *93*, 144404.
[40] X. Li, J.-T. Lü, J. Zhang, L. You, Y. Su, E. Y. Tsymbal, *Nano Lett.* **2019**, *19*, 5133.
[41] R. C. O'Handley, *Modern Magnetic Materials: Principles and Applications*, 1st ed.,Wiley-Interscience, New York **1999**.
[42] A. Kabir, J. Hu, V. Turkowski, R. Wu, R. Camley, T. S. Rahman, *Phys. Rev. B* **2015**, *92*, 054424.
[43] V. L. Deringer, A. L. Tchougréeff, R. Dronskowski, *J. Phys. Chem. A* **2011**, *115*, 5461.
[44] G. Kresse, D. Joubert, *Phys. Rev. B* **1999**, *59*, 1758.
[45] P. E. Blöchl, *Phys. Rev. B* **1994**, *50*, 17953.
[46] G. Kresse, J. Furthmüller, *Phys. Rev. B* **1996**, *54*, 11169.
[47] G. Kresse, J. Furthmüller, *Comput. Mater. Sci.* **1996**, *6*, 15.
[48] G. Kresse, J. Hafner, *Phys. Rev. B* **1993**, *47*, 558.
[49] G. Kresse, J. Hafner, *Phys. Rev. B* **1994**, *49*, 14251.
[50] J. P. Perdew, A. Zunger, *Phys. Rev. B* **1981**, *23*, 5048.
[51] S. Grimme, J. Antony, S. Ehrlich, H. Krieg, *J. Chem. Phys.* **2010**, *132*, 154104.
[52] S. Grimme, S. Ehrlich, L. Goerigk, *J. Comput. Chem.* **2011**, *32*, 1456.
[53] J. P. Perdew, K. Burke, *Phys. Rev. Lett.* **1996**, *77*, 3865.
[54] S. L. Dudarev, G. A. Botton, S. Y. Savrasov, C. J. Humphreys, A. P. Sutton, *Phys. Rev. B* **1998**, *57*, 1505.
[55] R. Dronskowski, P. E. Blöchl, *J. Phys. Chem.* **1993**, *97*, 8617.
[56] S. Maintz, V. L. Deringer, A. L. Tchougréeff, R. Dronskowski, *J. Comput. Chem.* **2013**, *34*, 2557.
[57] S. Maintz, V. L. Deringer, A. L. Tchougréeff, R. Dronskowski, *J. Comput. Chem.* **2016**, *37*, 1030.
[58] J. Taylor, H. Guo, J. Wang, *Phys. Rev. B* **2001**, *63*, 245407.
[59] M. Brandbyge, J. L. Mozos, P. Ordejón, J. Taylor, K. Stokbro, *Phys. Rev. B* **2002**, *65*, 165401.
[60] N. Troullier, J. L. Martins, *Phys. Rev. B* **1991**, *43*, 1993.
[61] M. Büttiker, Y. Imry, R. Landauer, S. Pinhas, *Phys. Rev. B* **1985**, *31*, 6207.

